

Evolutionary Algorithm Optimization of Staggered Biological or Biomimetic Composites Using the Random Fuse Model

*Original*

Evolutionary Algorithm Optimization of Staggered Biological or Biomimetic Composites Using the Random Fuse Model / Costagliola, Gianluca; Guarino, Roberto; Bosia, Federico; Gkagkas, Konstantinos; Pugno, Nicola M.. - In: PHYSICAL REVIEW APPLIED. - ISSN 2331-7019. - 13:3(2020), p. 034049. [10.1103/PhysRevApplied.13.034049]

*Availability:*

This version is available at: 11583/2809334 since: 2020-04-07T10:05:31Z

*Publisher:*

AMER PHYSICAL SOC

*Published*

DOI:10.1103/PhysRevApplied.13.034049

*Terms of use:*

This article is made available under terms and conditions as specified in the corresponding bibliographic description in the repository

*Publisher copyright*

(Article begins on next page)

# Evolutionary Algorithm Optimization of Staggered Biological or Biomimetic Composites Using the Random Fuse Model

Gianluca Costagliola<sup>1</sup>,<sup>2</sup>,<sup>3</sup> Roberto Guarino<sup>2</sup>,<sup>3</sup> Federico Bosia<sup>3</sup>,<sup>4</sup> Konstantinos Gkagkas,<sup>4</sup> and Nicola M. Pugno<sup>5,6,7,\*</sup>

<sup>1</sup>*Department of Physics, University of Torino, Via Pietro Giuria 1, Torino 10125, Italy*

<sup>2</sup>*École Polytechnique Fédérale de Lausanne (EPFL), Swiss Plasma Center (SPC), Villigen PSI CH-5232, Switzerland*

<sup>3</sup>*Department of Applied Science and Technology (DISAT), Politecnico di Torino, C.so Duca degli Abruzzi 24, Torino 10129, Italy*

<sup>4</sup>*Advanced Material Research Division, Toyota Motor Europe NV/SA, Hoge Wei 33B, Zaventem 1930, Belgium*

<sup>5</sup>*Laboratory of Bio-Inspired, Bionic, Nano, Meta Materials & Mechanics Department of Civil, Environmental and Mechanical Engineering, University of Trento, Via Mesiano, 77, Trento 38123, Italy*

<sup>6</sup>*School of Engineering and Materials Science, Queen Mary University of London, Mile End Road, London E1 4NS, United Kingdom*

<sup>7</sup>*Ket Lab, Edoardo Amaldi Foundation, Via del Politecnico snc, Rome 00133, Italy*

 (Received 3 May 2019; revised manuscript received 15 January 2020; accepted 31 January 2020; published 19 March 2020)

In Nature, biological materials such as nacre, bone, and dentin display an enhanced mechanical strength due to their structure characterized by hard inclusions embedded in a soft matrix. This structure has inspired the design of artificial materials with optimized properties. Thus, for given the mechanical properties of matrix and inclusions, it is fundamental to understand how the global observables, essentially strength, and ultimate strain are determined by the geometrical parameters of the inclusions. In this paper, we address this question by extending the two-dimensional random fuse model, which has been widely used to extract statistical properties of fracture processes, to the case of staggered stiff inclusions. We thus investigate numerically how emergent mechanical properties can be optimized by tuning geometrical dimensions and the arrangement of the inclusions. To do this, we adopt an optimization procedure based on an evolutionary algorithm to efficiently explore the parameter space and to determine the most favorable geometrical features of the inclusions for improved strength or ductility, or both. Various lattice sizes and volume fractions are considered. Depending on inclusion sizes and aspect ratios, composite strength or ultimate strain can be maximized, with the Pareto front for simultaneous optimization of the two being interpolated by a simple power law. Characteristic exponents for damage avalanche distributions are found to vary with respect to homogeneous structures, indicating increased fracture ductility simply due to optimized geometrical features. Our study indicates the possibility through structural optimization of creating staggered composites that allow significant advantages in terms of weight reduction and fuel consumption in automotive applications.

DOI: [10.1103/PhysRevApplied.13.034049](https://doi.org/10.1103/PhysRevApplied.13.034049)

## I. INTRODUCTION

Biological structural materials such as bones, teeth, and shells are characterized by exceptional mechanical strength and toughness due to their structure rather than the properties of the single components [1,2]. These biological materials display a hierarchical structure whose ultimate level at the nanoscale is characterized by stiff mineral inclusions embedded in a soft protein matrix [3–5]. In particular, the well-known staggered reinforcement architecture typical of nacre also recurs frequently in lower

volume fractions, e.g., in bone (30–50%) [6] or dentin (around 60%) [7]. Many studies have highlighted the effects due to this structure allowing the improvement of the global mechanical properties, fracture toughness [8–13], flaw tolerance, and strength [14–17], and also wear resistance [18,19].

These results have inspired research on artificial materials, aiming to reproduce staggered composite hierarchical structures with improved mechanical properties [20–28]. This type of composite can nowadays be realized using numerous techniques, including three-dimensional (3D) printing [29], freeze casting [30], vacuum-assisted magnetic alignment processes [31], or others. However, a

\*nicola.pugno@unitn.it

critical issue is to find the optimal structure for given elementary components, since not all the structures lead to an improvement of the mechanical properties. Geometrical design and size scales play a crucial role in many such artificial composite materials [32,33]. For example, it has been shown that a nacrelike structure realized with carbon nanotubes optimizes strength and toughness with exactly two hierarchical levels, just as natural nacre [34]. In Abid *et al.* [35], the discrete element method (DEM) was used to model a two-dimensional (2D) staggered composite structure, assessing the influence of geometrical parameters (aspect ratio, overlap ratio, and interface toughness) on the overall mechanical properties. The authors found that moderate statistical variations in the microstructure increase overall toughness, while larger variations lead to crack propagation along the weakest path, and a decrease in toughness. Thus, it is fundamental to set up a procedure to derive an optimal design, simultaneously maximizing the desired quantities, such as strength, toughness, and stiffness.

Many methods have been adopted to address the optimization of bio-inspired composite materials: Gu and co-authors employed a modified “greedy” algorithm [36] to optimize the toughness modulus of computer designed composite materials [37,38], in which the optimal geometric arrangement of stiff and soft building blocks is found to enhance the resistance to crack propagation. In more recent studies, machine-learning algorithms were used for this type of optimization [39,40]. In particular, a large set of training data was generated from the random combination of unit cells, whose mechanical properties were characterized by 2D finite-element simulations [41,42]. The results verified the strong potential of the machine-learning approach in predicting the mechanical properties of composite structures. In other approaches, ballistic finite-element simulations were used to optimize the impact resistance of a nacrelike composite using two objective functions: the flexural stiffness and the ballistic-penetration resistance of the considered armor [43].

In this paper, we conceptually investigate this issue by means of numerical simulations based on the random fuse model (RFM). In general, the RFM describes the fracture process of a material by exploiting the analogy between Hooke’s and Ohm’s laws, and has been widely studied in the literature [44,45]. Although the electrical-elastic analogy is an approximation, the RFM is well suited to describe fracture processes, especially in quasibrittle disordered media, where it has been shown to correctly reproduce the related phenomenology, e.g., power laws in the scaling of damage avalanches [46,47]. Moreover, we adopt this model because it can be easily implemented numerically and, at least in the 2D case, it is not too computationally expensive. This is essential to enable an optimization procedure requiring multiple repeated simulations. Despite providing an approximate description of a real fracture

process, the model is sufficiently general to give a qualitative picture of the main mechanisms taking place. A specific RFM formulation has been adopted in [48,49] to investigate mechanical properties of staggered composite materials, showing a good agreement with experimental observations. Thus, we expect that the RFM can also provide information regarding the optimal geometrical shape of staggered inclusions.

The RFM is implemented using a network of resistors with a statistical dispersion on their breaking thresholds and, in [49], a nacrelike structure is mimicked by modifying the lattice structure. For our purposes, we must adopt an alternative and more appropriate formulation. We use a regular square lattice of resistors representing the soft matrix, and stiff inclusions are simulated by increasing strength and stiffness in the corresponding lattice regions. Thus, we can explore the space of geometric parameters to find optimal configurations. Optimization is performed by using an evolutionary algorithm (EA) [50–52], which does not require extremely large training datasets, as in machine-learning algorithms. From these simulations, we deduce the optimal aspect ratio and arrangement of the staggered inclusions to be tested in experiments and we analyze their statistical properties.

The paper is organized as follows. In Sec. II, we describe the general formulation of the RFM and its extension to the case with staggered inclusions. In Sec. III, we describe the optimization algorithm and the strategy adopted in this particular case. In Sec. IV, we present optimization results and, in Sec. V, we analyze in detail some optimal configurations. In Sec. VI, we provide the conclusions.

## II. RANDOM FUSE MODEL

### A. General formulation

The random fuse model is implemented using a square lattice of  $L \times L$  resistors with conductivity  $c = 1$  [Fig. 1(a)]. A voltage difference  $V$  is applied along the horizontal direction between the two sides of the lattice, while periodic boundary conditions are set in the vertical direction. Each resistor has a breaking threshold  $x_j$  for the current, randomly extracted at the beginning of the simulation from a Weibull probability distribution  $W(x, \lambda, k) = k\lambda^{-1}(x/\lambda)^{k-1}e^{-(x/\lambda)^k}$  [53], where the scale parameter is  $\lambda = 1$  and the shape parameter is  $k = 2$ . Scaling laws and statistical results are not influenced by threshold distributions.

The Weibull distribution is a widespread choice to describe failure phenomena, e.g., for the fracture of brittle materials [46]. Moreover, it is a positive continuous function that is easy to handle analytically. Damage threshold distributions do not affect scaling laws since they are a universal feature of the physical phenomenon itself, and details of the starting disorder in the lattice do not

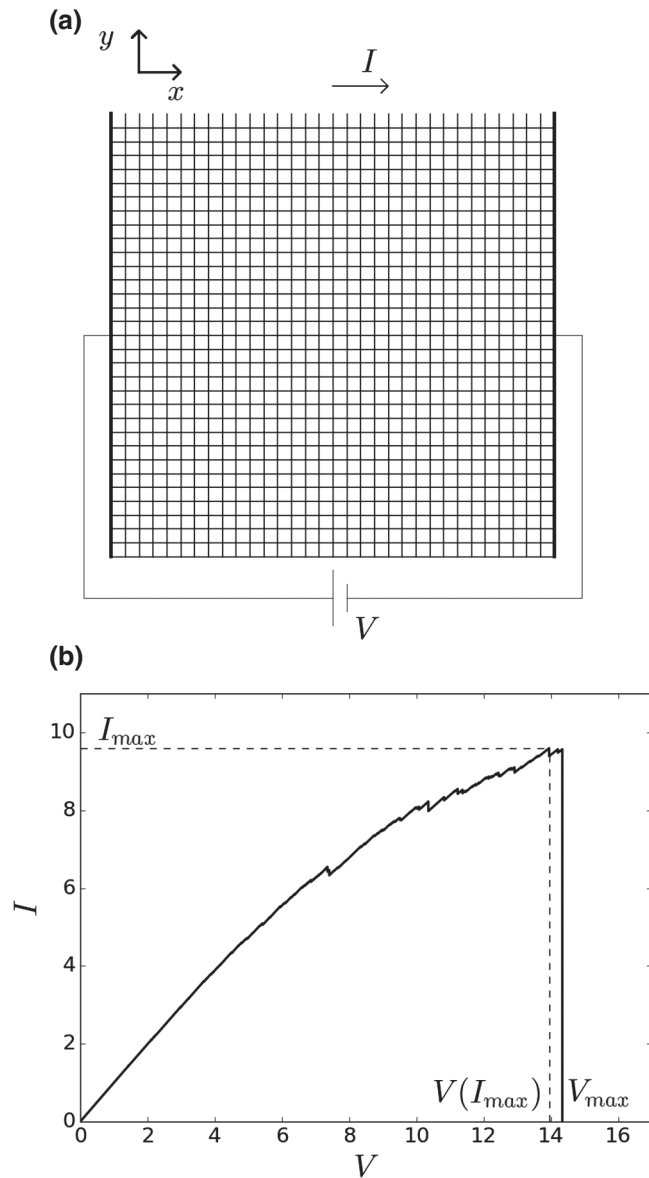


FIG. 1. (a) Schematic of the 2D lattice of resistors used in the RFM. (b) Characteristic  $I(V)$  plot with the notation used in the text obtained for  $L = 32$ ,  $\lambda = 1$ , and  $k = 2$ .

change the global power-law exponent. For many statistical observables, e.g., avalanche damage distributions, RFM exhibits universal power-law scaling, which is commonly found in fracture mechanics [54].

The algorithm is as follows. Starting from zero, the voltage is progressively increased by steps of  $\Delta V$ . At each step, the Kirchoff system of equations is solved to find the local currents  $I_j$  flowing in each resistor  $j$  and, consequently, the total current  $I$  flowing through the lattice. If some local currents  $I_j$  exceed the thresholds, the resistor with maximum ratio  $I_j/x_j$  is burnt and its conductivity is set to  $c = 0$ . The system of equations is solved again with the same voltage to find how the currents are redistributed on the whole

lattice. This procedure is repeated until there are no more resistors whose threshold is exceeded. After this, the voltage is increased by another step  $\Delta V$  and the algorithm is repeated. The overall system fails when a fracture of broken resistors crosses the whole lattice and the total current drops to zero.

Thus, in a single run we obtain a characteristic  $I(V)$  curve [Fig. 1(b)] showing the total current as a function of the voltage. From this curve, various observables can be extracted: the peak value is the maximum current  $I_{\max}$ , the corresponding voltage of the peak is  $V(I_{\max})$ , while the maximum voltage is  $V_{\max}$ . The total dissipated energy  $e$  corresponds to the area under the curve, i.e.,  $e = \int I(V)dV$ . Due to the random distribution of the thresholds, a reliable estimate of the observables requires repeated simulations. We denote with  $\langle \dots \rangle$  the statistical average of any observable obtained from RFM simulations.

The model and tools for result analysis are implemented with an in-house code written in c++. The Kirchoff system of equations is expressed in matrix form and solved by means of the c++ open-source library Armadillo embedded in the code. This is the most time-consuming operation, which depends on  $L$ . For this reason, the lattice side must be chosen according to the computational time and the number of repetitions required to achieve the desired precision. We will specify lattice side and repetitions for each individual case. Scaling laws with  $L$  are known in the literature [46].

In the following, we will adopt the terminology of the corresponding mechanical system, so that we will use the terms *strain*  $V$  to indicate the applied voltage, *stress*  $I$  to indicate the current, and *strength* for the maximum current  $I_{\max}$ . Moreover, the conductivity is analogous to the stiffness, and the total stiffness  $K$  of the system can be calculated as the angular coefficient of the  $I(V)$  curve before any rupture occurs.

## B. Staggered inclusions

We consider a 2D material with rectangular staggered inclusions, since they can be easily reproduced using a square lattice, and also to mimic the shape and arrangement of the lamellar structures found in real biological materials with variable volume fractions. Here, we consider a 2D model, but a possible implementation of a 3D RFM would be possible, although more computationally expensive. The present model represents, from a mechanical point of view, a plane-stress assumption, so that out-of-plane components of the crack propagation path are neglected. However, the results discussed are not expected to differ qualitatively in a 3D implementation.

The fracture process in this material can be qualitatively simulated with the RFM by setting a higher conductivity of the links on the lattice corresponding to the inclusions, which corresponds to a greater stiffness. Thus, we set their

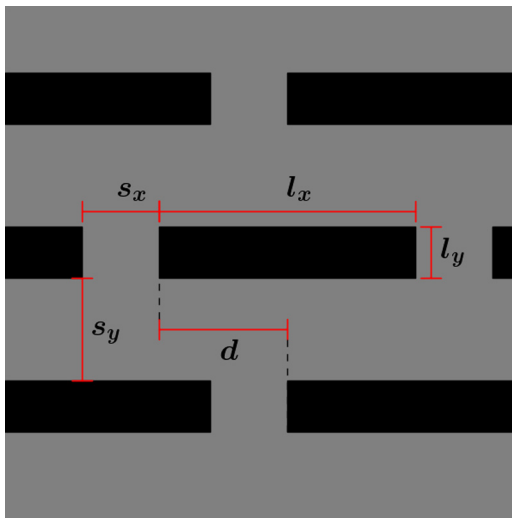


FIG. 2. Example of a portion of a 2D material with a matrix (gray) and the staggered inclusions (black), which are characterized by the five variables adopted in the text: inclusion lengths  $l_x$ ,  $l_y$ , their spacings  $s_x$ ,  $s_y$ , and offset  $d$ .

conductivity to  $c = 10$ , while in the matrix, i.e., the rest of the lattice,  $c = 1$ . Similarly, the rupture thresholds of these links are increased and their scale parameter is  $\lambda' = 10\lambda$ , while the shape parameter remains the same. Staggered inclusions are defined by five variables: lateral dimensions  $l_x$ ,  $l_y$ , their distances  $s_x$ ,  $s_y$  along the  $x$ ,  $y$  axes, respectively, and their offset  $d$  that characterizes the shift between two adjacent rows of inclusions, as illustrated in Fig. 2. Due to the discretization on a square lattice, these variables can only assume integer values. The volume fraction  $v$  of a configuration is defined as the ratio between the areas of the inclusions over the total area. In RFM, this can be related to the ratio between the links of the lattice belonging to inclusions over the total links.

In Fig. 3, we show the simulation results for a homogeneous and a staggered reinforcement structure. For this simulation only, all matrix conductivities in the homogeneous case have been adjusted so that the total stiffness at the beginning is the same as the staggered reinforced lattice. In the latter case, fracture propagation is forced to follow a winding path around the inclusions, so that the strength and ultimate strain are both enhanced.

It is important to note that, by modifying the stiffness of the homogeneous case, the strength does not change, but the ultimate strain decreases by increasing  $c$ . For example, in a uniform system composed only by the matrix, i.e.,  $c = 1$ , the ultimate strain is larger than both cases of Fig. 3. This is because the rupture thresholds are set on the local stress, so that by increasing the link conductivity, its rupture occurs at smaller strain values. For this reason, in the RFM, stiffer inclusions always reduce the overall ultimate strain with respect to a homogeneous

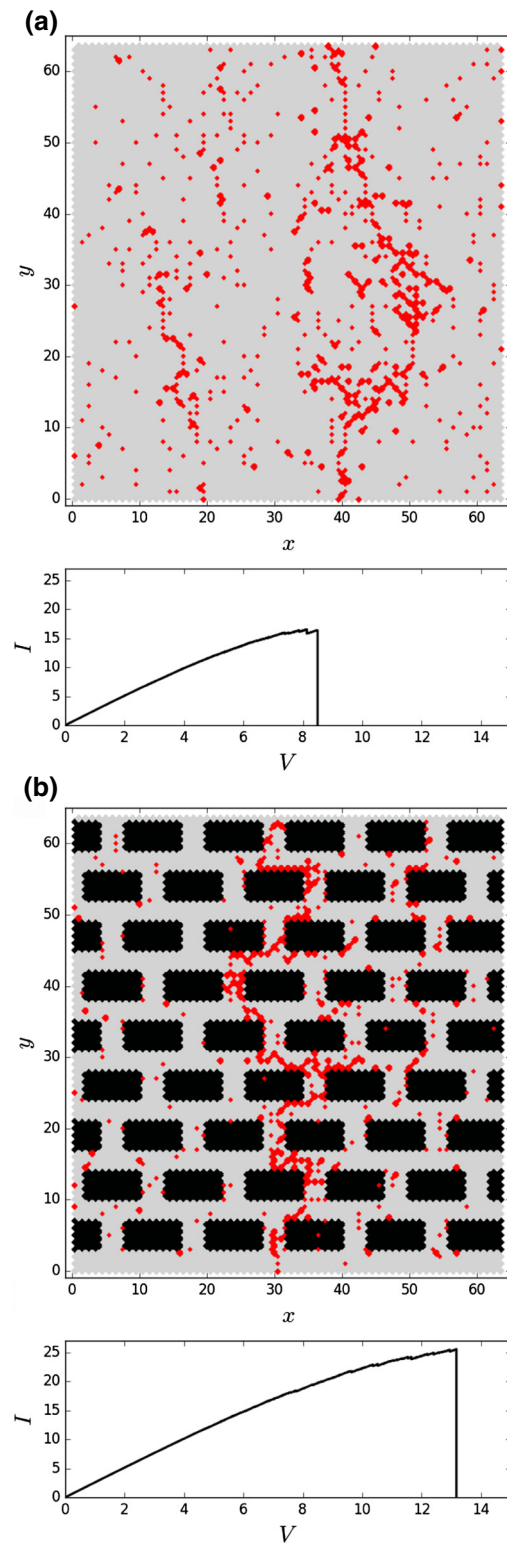


FIG. 3. (a) Final configuration after breakdown of the homogenized lattice with broken resistors in red (upper panel) and the corresponding stress-strain plot (lower panel) after a RFM simulation with  $L = 64$ . (b) The same plots for a RFM simulation on a lattice with staggered inclusions (highlighted in black), with  $l_x = 8$ ,  $l_y = 4$ ,  $s_x = 4$ , and  $s_y = 3$  in lattice units.

lattice only constituted by the matrix. Thus, an optimization tool is needed to determine the set of parameters ( $I_x$ ,  $I_y$ ,  $s_x$ ,  $s_y$ ,  $d$ ) leading to maximum strength and ultimate strain. Constraints and optimization details are discussed in Sec. III.

### III. OPTIMIZATION ALGORITHM

The optimization is performed using the software EASY [55–58] that is a generalized EA-based search tool. In a language borrowed from natural genetics, optimal solutions are progressively selected from a population of individuals according to the most successful in fitting the optimization criteria. Thus, an EA-based optimization starts from a given population and, by running the evaluation tool (in our case the RFM), its individuals are associated with their own “cost” value calculated in terms of the quantities to be optimized. Then, individuals are selected according to their fitness for the production of offspring, i.e., new solutions, and offspring is mutated with a certain probability, mimicking the natural processes of recombination and mutation. The cost value of offspring individuals is evaluated and they are included in the population replacing the parents, producing a new generation. This cycle is performed until the optimization criteria are met or the fixed maximum computational time is reached, so that the final output is a set of optimal solutions.

The use of an EA is well adapted to the problem analyzed in this paper, since it inherently allows multiobjective optimization. Further, it is more appropriate than gradient-based methods in determining a global optimum (thus avoiding local minima), especially in the present case where the configuration space is sparsely populated. Computation times essentially depend on repeated RFM simulations, so the algorithm itself is not too computationally demanding. A more detailed description of the latter is reported in Appendix A.

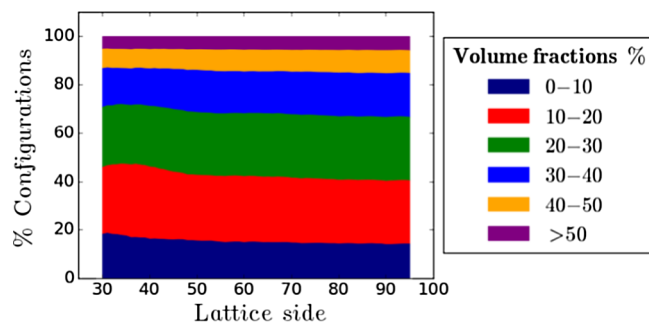


FIG. 4. Percentage of configurations arising for variable lattice side  $L$  and corresponding volume fraction  $v$ . The range for  $v$  is a strong constraint, since many configurations tested during the optimization fall outside the prescribed bounds and can be discarded, especially for larger  $v$  values.

In this optimization process, we adopt a ( $\mu_{EA}$ ,  $\lambda_{EA}$ ) EA scheme, where  $\mu_{EA}$  and  $\lambda_{EA}$  are the parent and the offspring population sizes, respectively. In the EASY setup panel, the Gray binary coding option is adopted: using standard binary coding, the representation of two

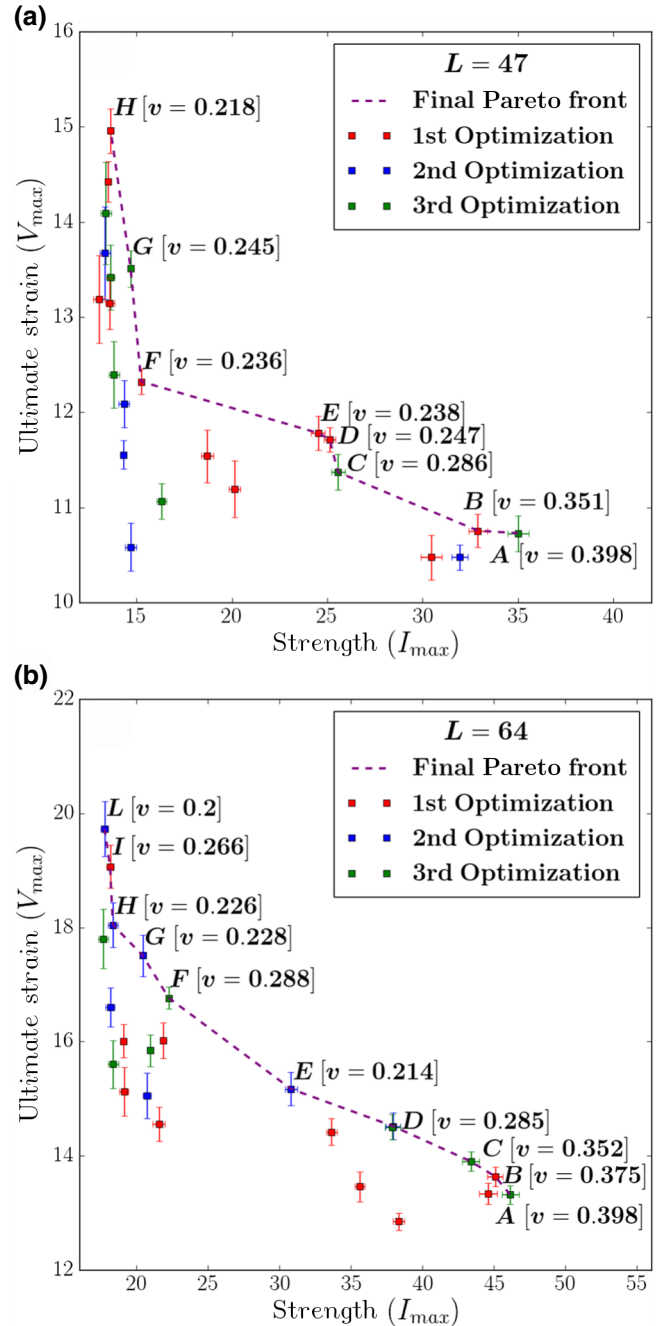


FIG. 5. Final optimization results for  $L = 47$  (a) and  $L = 64$  (b) in a  $I_{\max}$ - $V_{\max}$  plot, obtained after three optimization steps. The best configurations are labeled with a capital letter and connected by a dashed line, corresponding to the Pareto front. Their volume fraction  $v$  is reported in square brackets. Geometric parameters and observables of these configurations are reported in Tables I and II.

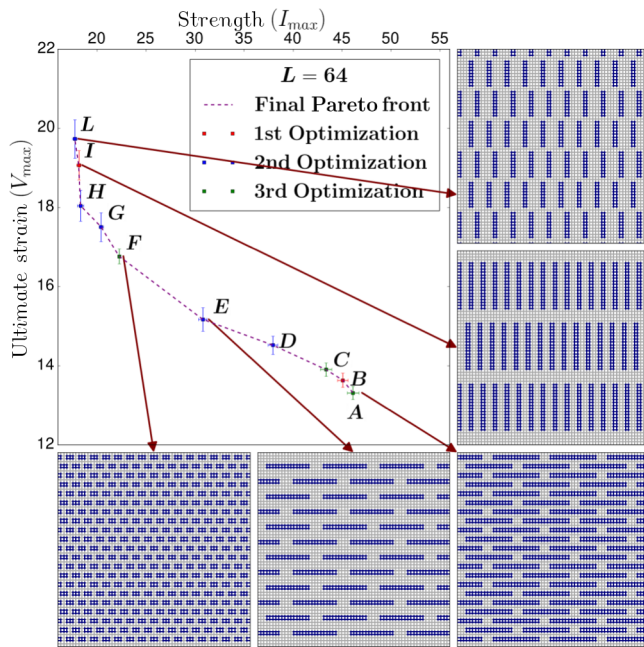


FIG. 6. Final optimal configurations and their representation on the lattice for  $L = 64$  and  $20\% < v < 40\%$ . Staggered inclusions are depicted as dark regions. Strain is applied along the horizontal direction, i.e.,  $x$  axis.

successive numbers (such as 011111 and 100000) may differ in many bits, while Gray coding uses an additional transformation to ensure that the representation of two successive numbers differs only by one bit, increasing the convergence rate of the algorithm [57]. The mutation probability is equal to 0.2 with a standard scheme, the crossover (recombination) probability is equal to 0.95 with a discrete scheme, and we employ a radial basis function (RBF) simple metamodel to improve the computational efficiency (see [58] for further information on the software).

We fix the offset  $d = (s_x + l_x)/2$ , as in staggered structures, so that the optimization procedure takes four input

variables:  $l_x, l_y, s_x, s_y$ . The optimization algorithm requires their ranges to be fixed, and we set  $1 \leq l_x, l_y \leq 15$ ,  $2 \leq s_x, s_y \leq 15$  in lattice units. Since these variables can assume only integer values, it is impossible to set a constraint on a fixed volume fraction. Thus, we set  $v$  in a range, for example  $v = 30\% \pm 10\%$ . During the optimization process, only configurations within this range of values are accepted.

Another possible option would be to fix the total Young's modulus, but we consider the problem from a manufacturing point of view, in which two specific materials are available for the soft matrix and inclusions with given elastic properties, to be combined with fixed density or weight constraints, corresponding to fixed volume fractions. This is important in the design of composites for the automotive sector, where density and weight must be carefully optimized. However, a study of the fixed stiffness and variable volume fraction is also addressed in Sec. IVC.

The fracture process is simulated by means of the RFM for a given variable set, so that output results are obtained. In the following optimizations, we aim to simultaneously maximize the observables  $I_{\max}$  and  $V_{\max}$ , i.e., the strength and ultimate strain, respectively. These are called objective variables. A given generic configuration  $S$  whose objective variables are  $I_S$  and  $V_S$  is an optimal solution if and only if

$$I_S = \max(I_{\max})|_{V_{\max}=V_S} \wedge V_S = \max(V_{\max})|_{I_{\max}=I_S}. \quad (1)$$

Equation (1) defines the so-called Pareto front, i.e., the set of optimal configurations.

In RFM simulations, all results have an error bar due to the statistical averages. This cannot be directly taken into account in the optimization algorithm, so that further postprocessing and data analysis are needed to check the validity of the optimized configurations. To reduce the probability of obtaining a false optimum due to statistical fluctuations, we increase the repetitions of the whole optimization process, using different starting configurations each time. In this way, a wider fraction of the variable

TABLE I. Characteristics of the configurations on the final Pareto front for  $L = 47$ , indicated with the capital letters of Fig. 5(a). For each configuration, the corresponding geometric variables and observables are reported (the brackets  $\langle \rangle$  are omitted): strength  $I_{\max}$ , ultimate strain  $V_{\max}$ , dissipated energy  $e$ , strain at maximum stress  $V(I_{\max})$ , stiffness  $K$ , and volume fraction  $v$ , respectively. For comparison, results for the homogeneous RFM are reported (configuration “S”). Uncertainties on the average values are reported in brackets.

Config.	$l_x$	$s_x$	$l_y$	$s_y$	$I_{\max}$	$V_{\max}$	$e$	$V(I_{\max})$	$K$	$v$
A	15	3	1	2	35.02(19)	10.73(55)	215(7)	10.2(2)	4.21	0.398
B	14	6	1	2	32.90(18)	10.75(48)	198(6)	10.2(2)	3.83	0.351
C	12	3	1	3	25.56(19)	11.37(36)	171(5)	10.8(3)	3.02	0.286
D	13	6	1	3	25.13(13)	11.71(29)	168(4)	11.3(1)	2.74	0.247
E	12	6	1	3	24.51(18)	11.78(36)	166(5)	11.6(2)	2.65	0.238
F	4	5	2	3	15.24(13)	12.32(12)	109(2)	12.1(1)	1.63	0.236
G	2	4	2	2	14.68(19)	13.51(14)	116(3)	13.2(2)	1.44	0.245
H	3	11	13	2	13.64(13)	14.96(23)	121(3)	14.7(2)	1.26	0.218
S					12.68(7)	16.91(15)	125(2)	16.6(2)	1.00	0

TABLE II. Characteristics of the configurations on the final Pareto front for  $L = 64$ , indicated with the capital letters of Fig. 5(b). The notation is the same as in Table I.

Config.	$l_x$	$s_x$	$l_y$	$s_y$	$I_{\max}$	$V_{\max}$	$e$	$V(I_{\max})$	$K$	$v$
A	15	4	1	2	46.1(6)	13.31(16)	343(8)	12.89(19)	4.25	0.398
B	14	5	1	2	45.1(5)	13.63(18)	342(8)	13.35(19)	4.00	0.375
C	14	6	1	2	43.4(6)	13.90(17)	337(8)	13.32(21)	3.82	0.352
D	15	5	1	3	37.9(5)	14.52(23)	310(9)	14.15(22)	3.21	0.285
E	14	5	1	4	30.8(4)	15.17(29)	267(9)	14.89(30)	2.55	0.214
F	2	2	1	2	22.4(1)	16.76(19)	215(4)	16.53(19)	1.73	0.288
G	2	3	1	2	20.4(2)	17.51(36)	208(7)	17.23(34)	1.54	0.228
H	2	6	4	2	18.3(3)	18.04(39)	190(7)	17.75(54)	1.31	0.226
I	1	3	15	5	18.1(2)	19.07(37)	198(7)	18.75(30)	1.23	0.266
L	1	5	8	2	17.7(2)	19.73(49)	202(8)	19.68(49)	1.17	0.200
S					16.70(5)	21.66(10)	208(2)	21.39(40)	1.00	0

space is explored, since the limited range set for  $v$  is a strong constraint, reducing the number of allowable configurations, as shown in Fig. 4. The final Pareto front is obtained by reporting all optimization results in the same plot  $I_{\max}$ - $V_{\max}$ , and the final optimal configurations are only those for which Eq. (1) still holds. We find that three repetitions of the whole optimization process are sufficient to identify the set of optimal configurations in the  $I_{\max}$ - $V_{\max}$  plot, since no substantial improvements are found with further optimization steps.

In the following, for each single optimization process, we set 120 exact evaluations of the RFM, with  $\mu_{\text{EA}} = 12$  and  $\lambda_{\text{EA}} = 6$  for each generation, and a random starting sample of configurations within the chosen range for  $v$ .

## IV. OPTIMIZATION RESULTS

### A. Volume fraction 20% < $v$ < 40%

We perform the simulations for two lattice lateral dimensions,  $L = 47$  and  $L = 64$ . These values are a compromise between acceptable computational costs, a good statistical significance, and the elimination of effects due to small lattice size. We apply the optimization strategy described in Sec. III by repeating multiple times the optimization procedure for each case. Results are shown in Fig. 5. Due to discretization issues, it is impossible to exactly maintain constant  $v$  values for varying  $L$  values. For this reason, optimal geometrical parameters depend on  $L$ , and optimal configurations for  $L = 47$  are not in general optimal for  $L = 64$ .

We can identify three classes of optimal configurations: those maximizing strength, whose inclusions are narrow and elongated along the  $x$  axis; those maximizing the ultimate strain, whose inclusions are elongated along the  $y$  axis; and those mixing the two features, whose inclusions are small and squarelike. A configuration with maximum strength is always obtained by setting a maximum  $p_x$  and

a minimum  $p_y$  within the allowed range, and by adjusting  $s_x, s_y$  to fall in the chosen volume fraction range. A configuration with maximum ultimate strain, instead, does not necessarily occur for a maximum  $p_y$  and a minimum  $p_x$ , as in this case for  $L = 47$ . Thus, for this value an optimization is required to find the optimal solution given the constraints. Lattices with optimal solutions for  $L = 64$  are shown in Fig. 6.

In Tables I and II, observables for all optimal configurations for both lattices are reported. As expected from considerations in Sec. IIB, the ultimate strain is inversely proportional to the global stiffness. Energy dissipation, corresponding to fracture toughness, assumes a maximum value for configurations with maximum strength, and a minimum for squarelike configurations in the middle of the Pareto front. Thus, if energy dissipation maximization is also required, configurations at the extreme of the Pareto front are preferable.

In Fig. 7(a), we report results of the same optimization procedures for  $L = 47$  with an offset  $d = 0$ , e.g., inclusions are arranged in a nonstaggered mesh. For all the optimal configurations with  $d = 0$ , both strength and ultimate strain are reduced with respect to the optimal staggered reinforcement configurations. We observe that optimal configurations obtained in the staggered reinforcement case do not correspond to optimal solutions for the case  $d = 0$ ; however, this difference could be ascribed to boundary effects, since similar qualitative configurations are found on the final Pareto front.

In Fig. 7(b), results are shown for an offset  $d' = (l_x + s_x)/4$  that is a compromise between a staggered and a nonstaggered structure. In this case, the Pareto front lies between those obtained in the previous cases, and optimal solutions display a comparable ultimate strain but smaller strength with respect to the staggered case. From these results, we deduce that, to maximize the strength, a staggered structure is crucial. This also holds for smaller volume fractions than those of real nacre: optimized

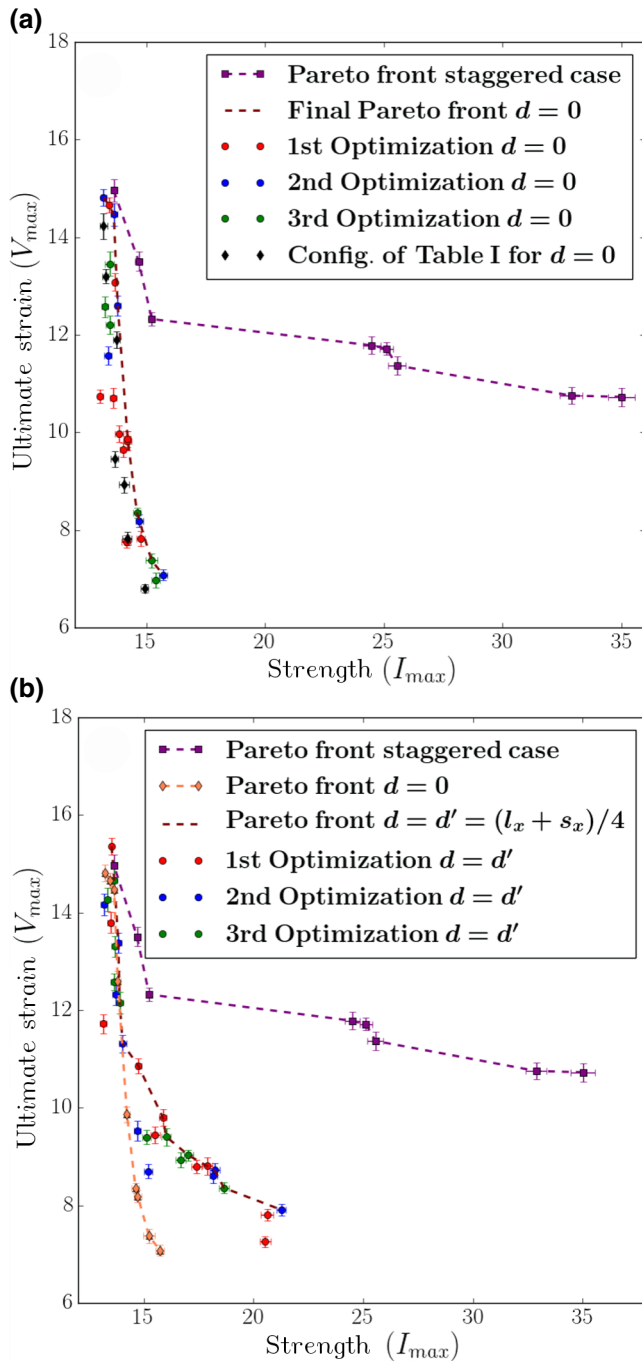


FIG. 7. (a) Pareto front obtained by combining three optimization processes to simultaneously maximize strength and ultimate strain in the case of  $d=0$ . For comparison, we report the Pareto front of Fig. 5(a), whose solutions display both larger strength and strain. Optimal configurations of Table I recalculated for  $d=0$  are no longer optimal solutions. (b) Comparison between the staggered-reinforcement Pareto front and those obtained for  $d=0$  and  $d=d'=(l_x+s_x)/4$ .

inclusions in a brick-and-mortar structure must have an elongated shape for maximum strength, while to achieve optimal ultimate strain values, other values of  $d$  can be considered.

## B. Volume fraction $v < 20\%$

We now perform the same optimization procedure as in the previous section but reducing the allowed volume fraction to  $v < 20\%$  for a lattice side  $L=64$ . This range could be useful to find optimal configurations of composite materials with a minimum amount of stiff inclusions. The optimal configurations are shown in Fig. 8 and their observables and geometric parameters are listed in Table III. In order to obtain optimal strength, the scenario of the previous section is confirmed: geometric variables must be set to a maximum  $p_x$  and a minimum  $p_y$  within the allowed range, while spacings  $s_x, s_y$  must be adjusted to fit the  $v$  constraint. In order to maximize ultimate strain, narrow inclusions elongated along the  $y$  axis must be adopted, but not necessarily with a maximum  $p_y$ . In particular, in configuration H of Table III, we obtain the nominal ultimate strain of the homogeneous case, which is the best achievable value. Again, the minimum energy configurations are those located at the centre of the Pareto front.

## C. Configurations with minimum spacings

We consider configurations with minimum spacings  $s_x, s_y$  between inclusions, which, in the context of RFM, is relevant to masonry structures. Thus, we fix  $s_x=s_y=2$  and we perform the optimization procedure only on the geometric variables  $p_x, p_y$ , without constraints on the volume fraction  $v$ . Results are shown in Fig. 9 and configurations are reported in Table IV. Again, in order to maximize

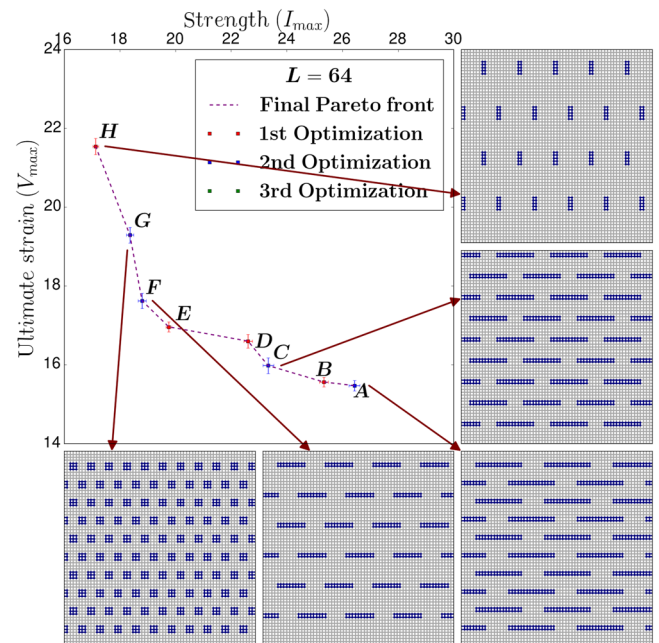


FIG. 8. Final optimal configurations and their lattice representation obtained after three optimization steps for  $L=64$  and  $v < 20\%$ . Staggered inclusions correspond to dark regions. Strain is applied along the horizontal direction, i.e., the  $x$  axis.

TABLE III. Configurations on the final Pareto front for  $L = 64$  and  $v < 20\%$ , indicated with capital letters as in Fig. 8 and their main observables, using the same notation as in Table I.

Config.	$l_x$	$s_x$	$l_y$	$s_y$	$I_{\max}$	$V_{\max}$	$e$	$V(I_{\max})$	$K$	$v$
A	15	8	1	5	26.43(19)	15.47 (13)	231(4)	15.12(14)	2.11	0.156
B	13	7	1	5	25.34(16)	15.56 (12)	224(3)	15.23(13)	2.02	0.154
C	12	6	1	6	23.33(20)	15.97 (20)	214(5)	15.73(20)	1.87	0.144
D	12	6	1	7	22.61(16)	16.59 (18)	217(4)	16.27(19)	1.77	0.128
E	12	7	1	9	19.76(10)	16.96 (13)	195(3)	16.61(14)	1.52	0.092
F	9	7	1	9	18.80(15)	17.62 (19)	192(4)	17.38(20)	1.39	0.082
G	2	4	2	4	18.37(13)	19.29 (20)	207(4)	19.03(21)	1.27	0.157
H	1	11	4	11	17.13(11)	21.54 (21)	212(4)	21.28(21)	1.03	0.034
S					16.70(5)	21.66(10)	208(2)	21.39(40)	1.00	0

the total strength (ultimate strain), configurations with the maximum value of  $p_x$  ( $p_y$ ) and minimum  $p_y$  ( $p_x$ ) are required, which also give maximum volume fraction values. In these optimal configurations, one of the sides must assume the minimum value, while the other side determines the overall strength. We observe that the second configuration, ordered according to the maximum strain, is found for inclusions with the smallest aspect ratio. This is the configuration closest to a real masonry structure made of small bricks.

Analyzing the results, including those of Secs. IVA and IVB, we find that the points on the Pareto fronts can be interpolated by a power law function in the plane  $I_{\max}$ - $V_{\max}$ , i.e.  $V_{\max} \sim I_{\max}^{-\alpha}$ , with  $0.2 < \alpha < 0.7$ . The value of  $\alpha$  depends on the lattice size and the inclusion geometry. This relationship is not an intrinsic feature of the Pareto

front (see Appendix B for further details), but can help to establish a correlation between maximum strength and ultimate strain of optimal solutions. The stress-strain curves of this system can be approximated by a linear elastic law with brittle failure, similar to that shown in Fig. 3, so that  $I_{\max} \sim KV_{\max}$ . Since the global stiffness  $K$  can be theoretically estimated, the relation  $V_{\max} \sim I_{\max}^{-\alpha}$  leads to the approximate relations  $I_{\max} \sim K^{1/(1+\alpha)}$  and  $V_{\max} \sim K^{-\alpha/(1+\alpha)}$  for configurations on the Pareto front. Similar results hold for the dissipated energy  $e$ , determining the specimen toughness. Such results derived from analysis of the optimal solutions can help to estimate these fundamental quantities in the design of optimal solutions.

Moreover, starting from a trivial optimal solution, e.g., a configuration with narrow inclusions elongated along  $x$ , similar to configuration A of Tables I–III, the relationship  $V_{\max} \sim I_{\max}^{-\alpha}$  can help to estimate the increase of  $V_{\max}$  when reducing  $I_{\max}$  for all other optimal solutions on the Pareto front.

This can be useful in the design of nontrivial staggered-reinforcement composites. To quantify the possible impact of optimization procedures on composite materials with staggered inclusions, we consider the case of their application in the automotive parts. At present, typical vehicles are built using approximately 50% composites or plastics by volume, corresponding to 10% by weight. Our study indicates that (for intermediate ultimate strain values), optimization of the internal structure can lead to a 2.5 times strength increase (in traction, as considered in the simulations). This implies the possibility of reducing the cross sections of the composite parts by 2.5 times while leaving the strength unchanged, i.e., of reducing their volumes (and consequently mass) by about 4 times, given the well-known square-cube law. In terms of weight, for a typical vehicle of 1500 kg, of which about 150 kg is plastics or composites, this means a reduction of more than 100 kg, which corresponds to a decrease in fuel consumption of over 1200 liters over 200,000 km, with the corresponding reduction in greenhouse gas emissions [59].

Finally, as shown in Fig. 14, if we consider only solutions with the stiffness  $K$  in a fixed range, the whole set

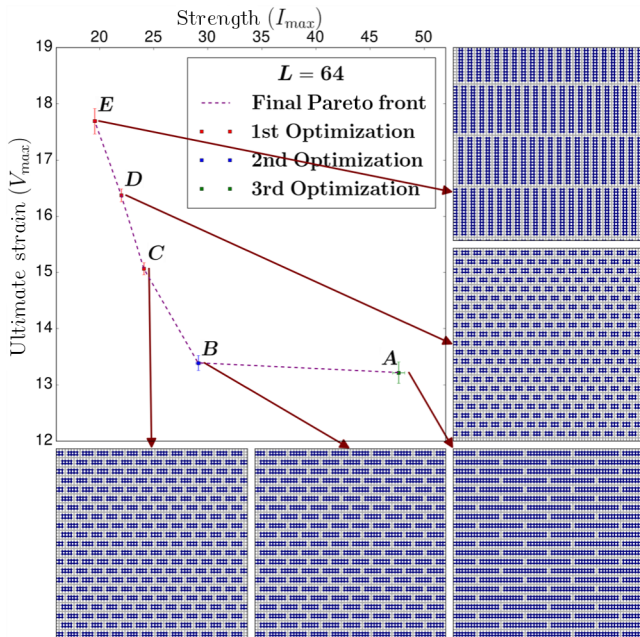


FIG. 9. Final optimal configurations of the Table IV, with the same notation as in Fig. 6.

TABLE IV. Table of optimal configurations with minimum spacings for  $L = 64$ , indicated with capital letters of Fig. 9 and the same notation as in Table I.

Config.	$l_x$	$s_x$	$l_y$	$s_y$	$I_{\max}$	$V_{\max}$	$e$	$V(I_{\max})$	$K$	$v$
A	14	2	1	2	47.65(55)	13.22(19)	360(10)	12.84(22)	4.60	0.443
B	5	2	1	2	29.13(23)	13.39(13)	224(4)	13.10(16)	2.78	0.375
C	3	2	1	2	24.10(13)	15.07(11)	210(3)	14.76(12)	2.09	0.325
D	2	2	1	2	22.01(10)	16.37(12)	207(3)	16.17(12)	2.88	0.273
E	1	2	15	2	19.56(16)	17.69(22)	198(4)	17.57(24)	1.42	0.448
S					16.70(5)	21.66(10)	208(2)	21.39(40)	1.00	0

of solutions in the  $I_{\max}$ - $V_{\max}$  plot is divided into parallel bands corresponding to stiffness ranges, each including some solutions falling on the Pareto front. From this, we deduce that each fixed stiffness range can capture only a limited segment of the Pareto front. This is because the stress-strain curve can be approximated by the relation  $I_{\max} = KV_{\max}$ , so that optimizing one variable (e.g., stress) with a fixed  $K$  leads to the optimization of the other (e.g., strain), making a simultaneous optimization of two objective variables unnecessary. In other words, as a first approximation, for each fixed  $K$  value, there is only one optimal solution, corresponding to the intersection of the line  $I_{\max} = KV_{\max}$  and the theoretical Pareto front of the total solution set.

## V. STATISTICAL PROPERTIES OF OPTIMAL SOLUTIONS

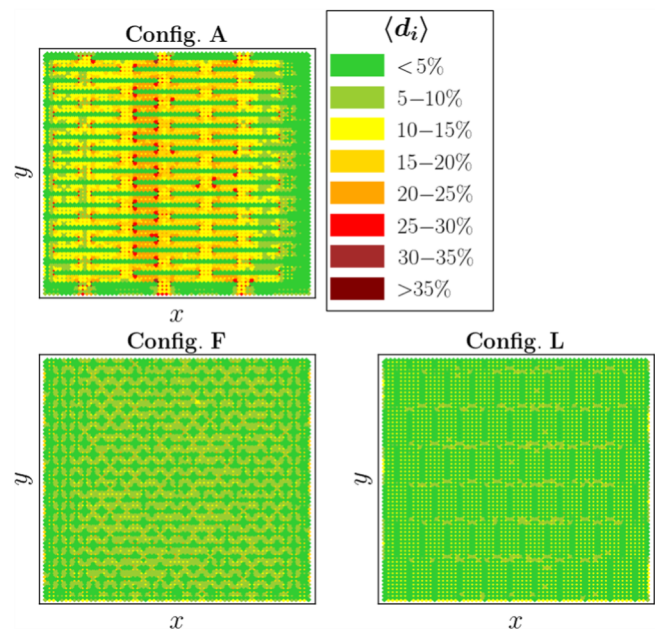
In this section, we focus on particular optimal solutions obtained in Sec. IVA with  $L = 64$ , to investigate their statistical properties in the RFM framework. We consider configurations A, F, and L of Table II, representing the three main types of inclusion: narrow and elongated along the  $x$  axis (A, with  $p_x = 15$ ,  $p_y = 1$ ,  $s_x = 4$ ,  $s_y = 2$ ), narrow and elongated along the  $y$  axis (L, with  $p_x = 1$ ,  $p_y = 8$ ,  $s_x = 5$ ,  $s_y = 2$ ), small squarelike (F, with  $p_x = 2$ ,  $p_y = 1$ ,  $s_x = 2$ ,  $s_y = 2$ ). We denote with S the results of the homogeneous RFM (without inclusions).

At the end of a RFM simulation, we can assign to each link  $i$  the quantity  $d_i$ , whose values are 1 (0) if the link is broken (unbroken). The total damage of the lattice can be defined as  $d = 1/n_l \sum_i d_i$ , where  $n_l$  is the total number of links. The fracture length is defined as the fraction of links connecting two nodes of disjoint regions after the failure, namely  $l_f$ . For a perfect cut, in which only links belonging to the intersecting fracture line are broken,  $l_f = d$ , but in general  $l_f < d$ . In repeated simulations, the mean value  $\langle \dots \rangle$  of these quantities can be calculated.

In Fig. 10, we report the distribution on the lattice of  $\langle d_i \rangle$ , showing the regions with larger rupture probability. In a homogeneous case, ruptures are uniformly distributed, while in staggered-reinforcement configurations they are mainly distributed in the matrix in the proximity of inclusions, with a larger probability at inclusion corners, due

to the typical boundary stress concentrations. However, for configurations F and L, the distribution is quite uniform along the  $x$  axis, while configuration A displays an increased concentration at the center of the lattice. Damage spikes at inclusion corners are also increased. The explanation is that in configuration A, the final fracture is forced through a winding path around stretched inclusions along  $x$ , so that the center of the lattice is statistically crossed many times by a fracture line spanning the  $x$  direction.

For this reason, in configuration A, both the total damage and fracture length are increased with respect to S. On the other hand, for both configurations F and L, there is a slight reduction of the total damage, as shown in Fig. 11(a). This means that ruptures are concentrated around the main fracture line and their probability decreases in the rest of the matrix. We also note that for configuration L, whose maximum strain is close to S, the fracture length is reduced, which means that the structure with this type of inclusion reduces the tortuosity of the fracture propagation.

FIG. 10. Comparison of the average damage  $\langle d_i \rangle$  in the lattice for configurations A,F,L.

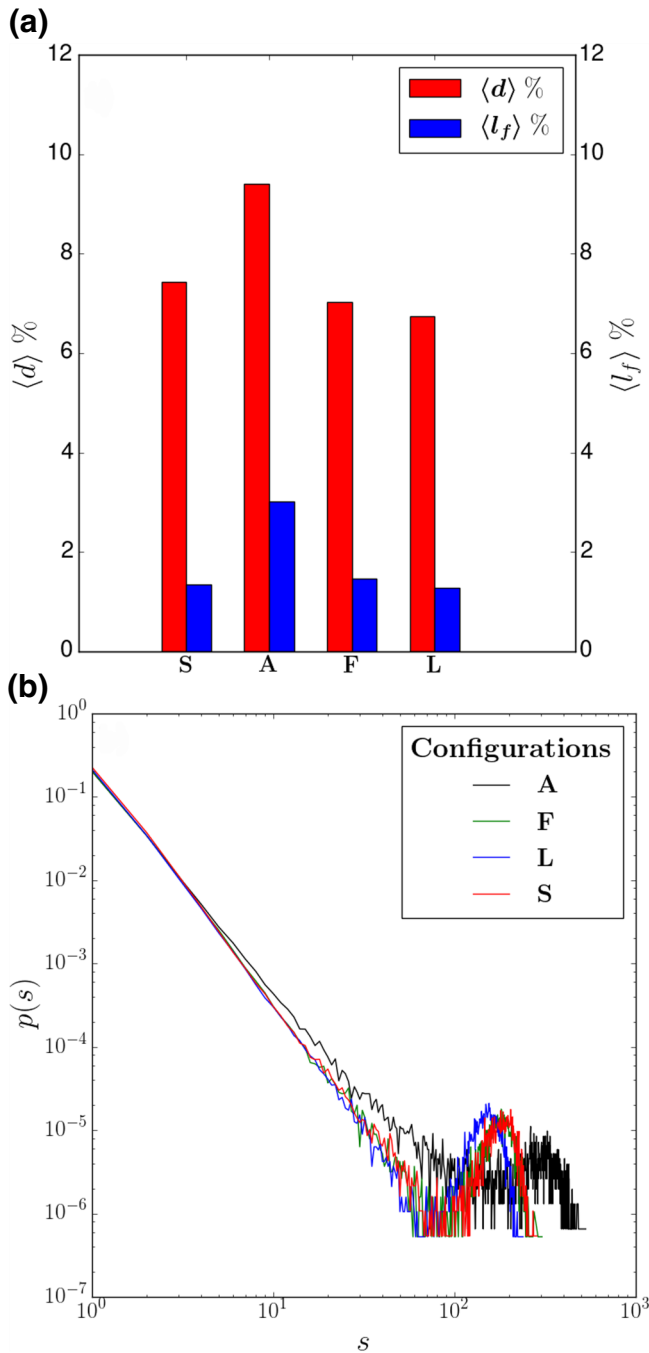


FIG. 11. (a) Comparison of the total damage  $\langle d \rangle$  and fracture length  $\langle l_f \rangle$  for the homogeneous case and the configurations A, F, and L. (b) Comparison of the avalanche distributions  $p(s)$  for configurations A, F, and L and the homogeneous case.

In Fig. 11(b), we report the calculated avalanche distributions. The number  $s$  of broken links for a given strain value corresponds to the size of a single avalanche event. In repeated simulations, the distribution  $p(s)$  of the avalanche sizes can be sampled, giving the occurrence probability of an avalanche of size  $s$ . In the homogeneous RFM,  $p(s)$  displays a decreasing power-law behavior with

a final peak due to the last catastrophic event involving many links [45]. Configurations F and L display small modifications with respect to S, while differences are found for configuration A: the slope of the power law is smaller, so that there is an increase of larger avalanche ruptures, and the peak of the final rupture is smaller. This is a consequence of the increased fracture toughness, which allows the presence of more ruptures in number and size before they trigger failure.

From this analysis, we find how different types of inclusions modify the global statistical properties of the system and the spread of damage. This could be useful in practical applications, where not only material strength, but also general material behavior at failure must be considered.

## VI. CONCLUSIONS

In this paper, we have applied the random fuse model to the evaluation of the mechanical properties of composite structures, characterized by thin staggered stiff inclusions embedded in a soft matrix, investigating the influence on global properties of the geometry and arrangement of inclusions. To do this, instead of analyzing geometrical structures found in nature, we started from given material properties and derived optimal geometrical configurations for chosen mechanical characteristics, thus linking their structure to an evolutionary optimization process that has taken place in biological structures. To determine optimal configurations, we used an EA-based tool to perform optimization procedures for different lattice sizes and volume fractions.

Our study confirms known results in the literature for staggered composite structures but also adds insight into variations on these geometries. Optimal solutions, which simultaneously maximize strength and ultimate strain according to Eq. (1), can be grouped into three main types:

(1) Structures with elongated inclusions along the direction of applied strain, which maximize the total strength up to a factor 3 with respect to the homogeneous case [Fig. 12(a)]

(2) Structures with elongated inclusions along an orthogonal direction to the applied strain, which maximize the ultimate strain up to the nominal maximum value of the homogeneous case. Here, contrary to the first case, the optimal configuration does not necessarily occur for a limiting value of the geometrical parameters within their allowed range. Instead, intermediate values can lead to optimal ultimate strain values, depending on lattice size and volume fraction [Fig. 12(b)]

(3) Structures with small inclusions of comparable side lengths (typically 2:1), which allow an increase of material strength with a limited reduction of ultimate strain with respect to the homogeneous case. This case is closer to

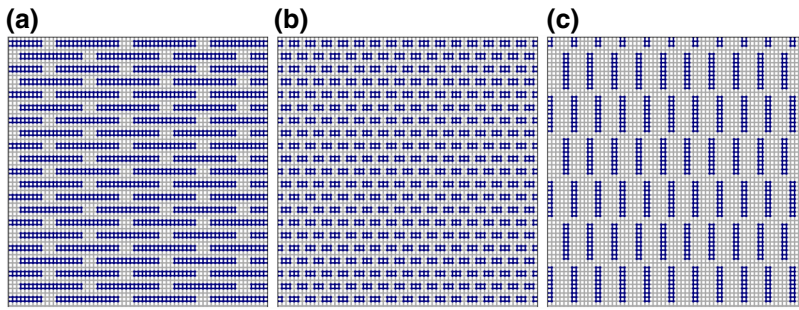


FIG. 12. Main types of optimal solutions highlighted in the conclusions.

a particle-reinforced composite, rather than a staggered-reinforcement structure [Fig. 12(c)]

In general, toughness is maximized by the first two types of structures, and the staggered arrangement is shown to be crucial to maximize strength, due to crack stopping effects. This analysis remains valid when varying the volume fraction of inclusions, which only influences the specific geometric parameters for each optimized geometry.

An important conclusion of this work is that the Pareto front resulting from the simultaneous optimization of strength and ultimate strain can be interpolated by a simple power law, providing useful empirical relations between these observables for optimal solutions.

We have also analyzed the statistical properties associated with these structures, in terms of fracture avalanche distributions, and in terms of spatial damage distributions under loading. These are important, since they are indicative of different universality classes, i.e., of a potential change of the underlying fracture mechanisms that can occur with structural modifications. For structures maximizing strength, the characteristic exponent of the fracture avalanche distribution is reduced with respect to the homogeneous case and the size of the catastrophic events at failure increases. This is due to increased fracture toughness, enabling larger rupture avalanches. Another consequence is the spatially nonuniform statistical distribution of damage in the lattice, suggesting that a further increase of the strength could be achieved by selectively reinforcing specific regions. For other types of configurations, it is possible to reduce the total damage and the fracture length with respect to the homogeneous case. These studies indicate that staggered inclusions could be exploited not only to increase the material strength, but also to modify statistical properties and fracture profiles by means of an appropriate geometric design. In future, we plan to adopt EA approaches to address these issues in three-dimensional models.

#### ACKNOWLEDGMENTS

G.C. is supported by the project “Metapp” (No. CSTO160004) funded by Fondazione San Paolo. F.B.

is supported by H2020 FET Open “Boheme” grant No. 863179 and by the project “Metapp” (No. CSTO160004) funded by Fondazione San Paolo. N.M.P. is supported by the European Commission under the Graphene Flagship Core 2 grant No. 785219 (WP14, “Composites”), the FET Proactive (“Neurofibres”) grant No. 732344, the FET Open (Boheme) grant No. 863179 as well as by the Italian Ministry of Education, University and Research (MIUR) under the “Departments of Excellence” grant L. 232/2016, the ARS01- 01384-PROSCAN and the PRIN-20177TTP3S grants. Computational resources were provided by the C3S centre at the University of Torino (c3s.unito.it). The software EASY was developed and provided by the Parallel CFD & Optimization Unit at National Technical University of Athens (NTUA). All authors would like to thank Kyriakos Giannakoglou and his group at NTUA for useful suggestions and discussions about optimization issues.

#### APPENDIX A: EVOLUTIONARY ALGORITHMS AND easy SOFTWARE CHARACTERISTICS

Evolutionary algorithms have been adopted for many complex problems in engineering, manufacturing, computer sciences, logistics, business, etc. They can handle multiobjective and multidisciplinary problems, where other traditional methods might fail in providing solutions. Genetic algorithms (GA) and evolution strategies (ES) are the two most widely used EAs. Advantages include, among others:

- (a) robustness
- (b) ability to avoid local optima and to locate the global optimal solution
- (c) ability to accommodate other analysis software in the search for optimal solutions
- (d) ability to locate feasible optimal solutions in optimization problems with constraints

Classical optimization methods are based on the approach of keeping the best obtained solution and attempting to improve it further, using deterministic or stochastic rules. This leads to the risk of obtaining solutions that depend on the starting guess, and the danger of converging to local rather global optima.

Instead of processing and improving only a single solution at a time, EAs maintain a population of several candidate solutions simultaneously. Separate analysis tools (in this work, the random fuse model) are used to determine the relative merit of each population member.

As in other EA approaches, in the adopted software (EASY) the individuals forming the current population compete and the most successful among them will have a relatively larger number of offspring in the next generation. Through encoded natural processes, fittest individuals increase their presence in the forthcoming generation, while unfit ones are likely to die out. The next generation is formed by breeding them together using operators borrowed from natural genetics. This process leads to the evolution of populations of individuals that are better suited to their environment than the individuals that they were created from, just as in natural adaptation. Thus, EA models natural processes, such as selection, recombination, and mutation. Thus, the most promising parts of the search space are explored by exploiting knowledge gained during previous explorations and the optimal solution is finally located. Basic EA phases are the formation of the initial starting population, generated through sampling randomly from the search space, the objective function that is used to judge the quality of the population members, as well as the process for creating offspring.

Practical problems often involve several noncommensurable or competing objectives that require simultaneous optimization. An optimal performance according to one objective often implies unacceptably low performance for one or more of the other objectives, creating the need for a compromise. To treat this, multiobjective problems are characterized by a family of noninferior, alternative solutions, known as the Pareto optimal front. The evolutionary algorithm used in this work may handle an unlimited number of objectives, providing a multidimensional Pareto front of optimal solutions as well as postprocessing tools to aid in making critical decisions.

It can also handle any number of constraints. Unfeasible solutions that emerge during the evolution process are penalized by reducing their fitness value in proportion to the degree of constraint violation, thus eliminating unfeasible solutions and providing optimal solutions or a front of optimal feasible solutions. To reduce simulation times, the software allows one to invoke the use of dynamically trained artificial neural networks, which require a minimum number of calls to the analysis tool and act as a surrogate model during the optimization.

An EA-based computation starts from a fixed number of individuals (the starting population), which are usually randomly generated according to the external constraints, in our case the volume fraction. In principle, the computation can start from any user-defined population, based for example on previous optimization procedures. From the first generation, the next is generated by

exploiting recombination and random mutation, both processes occurring with a given probability fixed by the user, as reported in Sec. III. The former encodes the production of offspring from two parents, obtained by means of a mathematical deterministic rule, e.g., a linear interpolation, allowing random jumps in the parameter space, in order to escape from local minima or possible unconnected parts of the domain.

A relevant part of the EA research is devoted to finding the most efficient recombination and mutation rules to apply to practical cases. In the EASY software, many rules can be selected (see references for details). In our cases, since input variables are integer numbers encoded by means of Gray binary coding, each solution is represented by a string of bits. The recombination of two parents is performed by dividing their bit string in half, and attaching the first half of one string with the second half of the other, so that two new strings, i.e., a double offspring, is generated. Instead, the mutation is performed by flipping from 0 to 1, or *vice versa*, the value of a bit randomly chosen in the new strings. The cost value of the offspring is then computed. If they are better solutions, they replace the parents in the next generation. This is done for all the individuals of a generation. This cycle is performed until the optimization criteria are met. In our case, we fix the total number of evaluations of the cost function, i.e., the RFM, to 120, as reported in Sec. III. This number should be chosen according to the computational time available. After these evaluations, the algorithm stops and the final optimal solutions are the best fits chosen among the last generation.

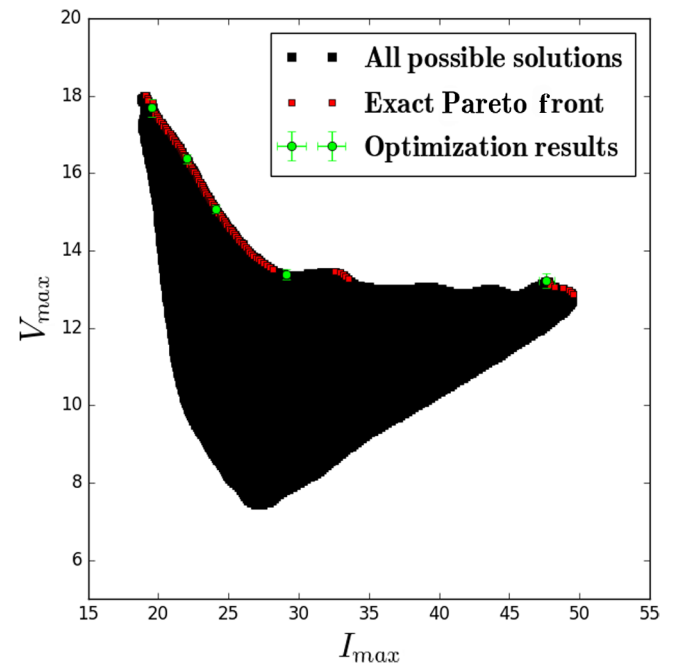


FIG. 13. Comparison between optimization results and a brute-force approach, in which the exact Pareto front is derived from the set of all solutions.

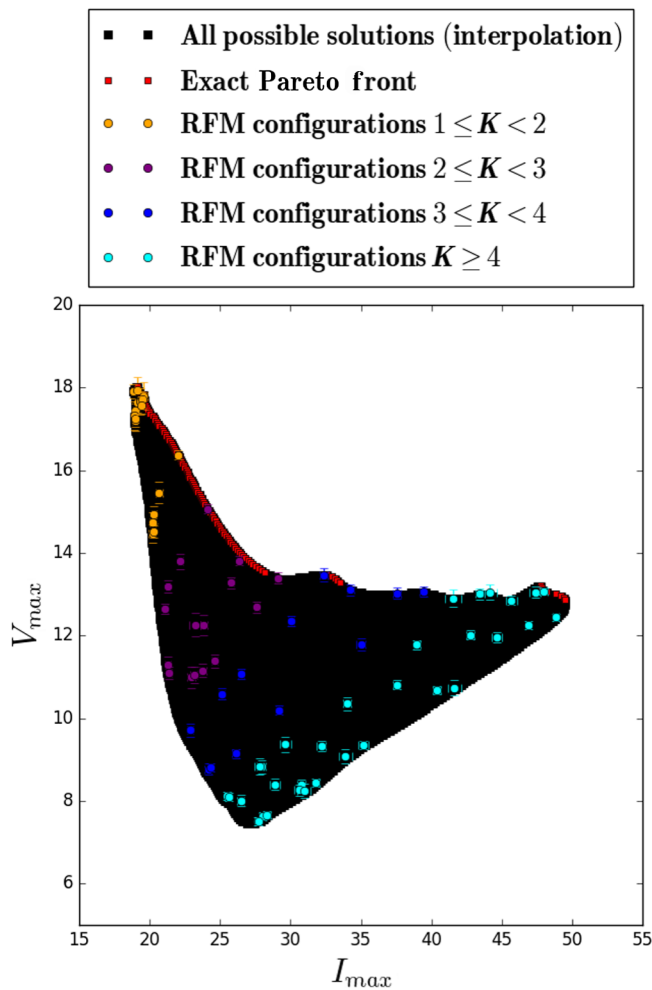


FIG. 14. Plot related to the discussion in Sec. IVC, showing the sets of configurations obtained for various fixed ranges of stiffness  $K$ , compared with the exact Pareto front and the total interpolated solution set.

## APPENDIX B: EXACT CALCULATION OF THE PARETO FRONT

In Sec. IVC, we considered configurations with fixed minimum spacings  $s_x, s_y$ , while optimizations were performed only for the inclusion lengths in the range  $1 < p_x, p_y < 15$ . In this case, it is possible to evaluate all configurations and calculate their observables with a “brute force” approach. Thus, we perform simulations for almost all possible staggered-reinforcement configurations and results for  $I_{\max}, V_{\max}$  are obtained. We extend these results to all real numbers  $(x, y)$  in the domain  $1 < x, y < 15$  by means of linear interpolation. Results are shown in Fig. 13, in a  $I_{\max}$ - $V_{\max}$  plot: the black area represents the set of the total possible results given by the interpolation. The red points represent the exact Pareto front, determined using the definition from (1). The latter has a nontrivial shape and is discontinuous. The green points represent the

optimization results from Sec. IVC, and clearly fall on the exact Pareto front, while small deviations are due to non-integer inclusion lengths, which cannot be captured by the RFM. This plot confirms the validity of the procedure used herein to find optimal solutions. In Fig. 14, we show the same plot highlighting the configurations in fixed ranges of stiffness.

- [1] B. Ji and H. Gao, Mechanical properties of nanostructure of biological materials, *J. Mech. Phys. Solids* **52**, 1963 (2004).
- [2] M. A. Meyers, P. Y. Chen, A. Y. M. Lin, and Y. Seki, Biological materials: Structure and mechanical properties, *Prog. Mater. Sci.* **53**, 1 (2008).
- [3] J. D. Currey, Mechanical properties of mother of pearl in tension, *Proc. R. Soc. London B* **196**, 443 (1977).
- [4] A. P. Jackson, J. F. V. Vincent, and R. M. Turner, The mechanical design of nacre, *Proc. R. Soc. London B* **234**, 415 (1988).
- [5] J. Sun and B. Bhushan, Hierarchical structure and mechanical properties of nacre: A review, *RSC Adv.* **2**, 7617 (2012).
- [6] I. Jäger and P. Fratzl, Mineralized collagen fibrils: A mechanical model with a staggered arrangement of mineral particles, *Biophys. J.* **79**, 1737 (2000).
- [7] B. Bar-On and H. D. Wagner, Enamel and dentin as multi-scale bio-composites, *J. Mech. Behav. Biomed. Mat.* **12**, 174 (2012).
- [8] S. Kamat, X. Su, R. Ballarini, and A. H. Heuer, Structural basis for the fracture toughness of the shell of the conch *Strombus gigas*, *Nature* **405**, 1036 (2000).
- [9] R. Z. Wang, Z. Suo, A. G. Evans, N. Yao, and I. A. Aksay, Deformation mechanisms in nacre, *J. Mater. Res.* **16**, 2485 (2001).
- [10] K. S. Katti, D. R. Katti, S. M. Pradhan, and A. Bhosle, Platelet interlocks are the key to toughness and strength in nacre, *J. Mater. Res.* **20**, 1097 (2005).
- [11] P. Fratzl, H. S. Gupta, F. D. Fischer, and O. Kolednik, Hindered crack propagation in materials with periodically varying young’s modulus—lessons from biological materials, *Adv. Mater.* **19**, 2657 (2007).
- [12] M. A. Meyers, A. Yu-Min Lin, P. Y. Chen, and J. Muiyco, Mechanical strength of abalone nacre: Role of the soft organic layer, *J. Mech. Behav. Biomed. Mater.* **1**, 76 (2008).
- [13] F. Barthelat and R. Rabiei, Toughness amplification in natural composites, *J. Mech. Phys. Solids* **59**, 829 (2011).
- [14] H. Gao, B. Ji, I. L. Jäger, E. Arzt, and P. Fratzl, Materials become insensitive to flaws at nanoscale: Lessons from nature, *Proc. Natl. Acad. Sci. USA* **100**, 5597 (2003).
- [15] H. Gao, B. Ji, M. J. Buehler, and H. Yao, Flaw tolerant bulk and surface nanostructures of biological systems, *Mechan. Chem. Biosyst.* **1**, 37 (2004).
- [16] F. Song and Y. L. Bai, Effects of nanostructures on the fracture strength of the interfaces in nacre, *J. Mater. Res.* **18**, 1741 (2003).
- [17] R. Guarino, S. Goffredo, G. Falini, and N. M. Pugno, Mechanical properties of *Chamelea gallina* shells at different latitudes, *J. Mech. Behav. Biomed. Mater.* **94**, 155 (2019).

- [18] P. Stempfle and M. Brendle, Tribological behaviour of nacre - influence of the environment on the elementary wear processes, *Tribol. Int.* **39**, 1485 (2006).
- [19] P. Stempfle, T. Djilali, R. K. Njiwa, M. Rousseau, E. Lopez, and X. Bourrat, Thermal-induced wear mechanisms of sheet nacre in dry friction, *Tribol. Lett.* **35**, 97 (2009).
- [20] G. Mayer, Rigid biological systems as models for synthetic composites, *Science* **310**, 1144 (2008).
- [21] H. D. Espinosa, J. E. Rim, F. Barthelat, and M. J. Buehler, Merger of structure and material in nacre and bone – Perspectives on de novo biomimetic materials, *Prog. Mater. Sci.* **54**, 1059 (2009).
- [22] G. M. Luz and J. F. Mano, Biomimetic design of materials and biomaterials inspired by the structure of nacre, *Philos. Trans. R. Soc. Math. Phys. Eng. Sci.* **367**, 1587 (2009).
- [23] F. Barthelat and D. J. Zhu, A novel biomimetic material duplicating the structure and mechanics of natural nacre, *J. Mater. Res.* **26**, 1203 (2011).
- [24] L. S. Dimas, G. H. Bratzel, I. Eylon, and M. J. Buehler, Tough composites inspired by mineralized natural materials: Computation, 3d printing, and testing, *Adv. Fun. Mater.* **23**, 4629 (2013).
- [25] J. Duan, S. Gong, Y. Gao, X. Xie, L. Jiang, and Q. Cheng, Bioinspired ternary artificial nacre nanocomposites based on reduced graphene oxide and nanofibrillar cellulose, *ACS Appl. Mater. Interfaces* **8**, 10545 (2016).
- [26] M. Farhadi-Khouzani, C. Schütz, G. M. Durak, J. Fornell, J. Sort, G. Salazar-Alvarez, L. Bergström, and D. Gebauer, A CaCO<sub>3</sub>/nanocellulose-based bioinspired nacre-like material, *J. Mater. Chem. A* **5**, 16128 (2017).
- [27] M. Grossman, D. Pivovarov, F. Bouville, C. Dransfeld, K. Masania, and A. R. Studart, Hierarchical toughening of nacre-like composites, *Adv. Funct. Mater.* **29**, 1806800 (2019).
- [28] F. Libonati, A. E. Vellwock, F. Ielmini, D. Abliz, G. Ziegmann, and L. Vergani, Bone-inspired enhanced fracture toughness of de novo fiber reinforced composites, *Sci. Rep.* **9**, 3142 (2019).
- [29] P. Zhang, M. A. Heyne, and A. C. To, Biomimetic staggered composites with highly enhanced energy dissipation: Modeling, 3D printing, and testing, *J. Mech. Phys. Solids* **83**, 285 (2015).
- [30] A. Dutta and S. A. Tekalur, Synthetic staggered architecture composites, *Mater. Des.* **46**, 802 (2013).
- [31] M. Grossman, F. Bouville, K. Masania, and A. R. Studart, Quantifying the role of mineral bridges on the fracture resistance of nacre-like composites, *Proc. Natl. Acad. Sci. USA* **115**, 12698 (2018).
- [32] I. Corni, T. J. Harvey, J. A. Wharton, K. R. Stokes, F. C. Walsh, and R. J. K. Wood, A review of experimental techniques to produce a nacre-like structure, *Bioinspir. Biomim.* **7**, 031001 (2012).
- [33] F. Barthelat, Designing nacre-like materials for simultaneous stiffness, strength and toughness: Optimum materials, composition, microstructure and size, *J. Mech. Phys. Solids* **73**, 22 (2014).
- [34] N. M. Pugno, Mimicking nacre with super-nanotubes for producing optimized super-composites, *Nanotechnology* **17**, 5480 (2006).
- [35] N. Abid, J. W. Pro, and F. Barthelat, Fracture mechanics of nacre-like materials using discrete-element models: Effects of microstructure, interfaces and randomness, *J. Mech. Phys. Solids* **124**, 350 (2019).
- [36] F. Dunstan and D. Welsh, A greedy algorithm for solving a certain class of linear programmes, *Math. Program.* **5**, 338 (1973).
- [37] G. X. Gu, L. Dimas, Z. Qin, and M. J. Buehler, Optimization of composite fracture properties: Method, validation, and applications, *J. Appl. Mech.* **83**, 071006 (2016).
- [38] G. X. Gu, S. Wettermarck, and M. J. Buehler, Algorithm-driven design of fracture resistant composite materials realized through additive manufacturing, *Add. Manuf.* **17**, 47 (2017).
- [39] R. Liu, A. Kumar, Z. Chen, A. Agrawal, V. Sundararaghavan, and A. Choudhary, A predictive machine learning approach for microstructure optimization and materials design, *Sci. Rep.* **5**, 11551 (2015).
- [40] K. T. Butler, D. W. Davies, H. Cartwright, O. Isayev, and A. Walsh, Machine learning for molecular and materials science, *Nature* **559**, 547 (2018).
- [41] G. X. Gu, C. T. Chen, and M. J. Buehler, De novo composite design based on machine learning algorithm, *Extr. Mech. Lett.* **18**, 19 (2018).
- [42] G. X. Gu, C. T. Chen, D. J. Richmond, and M. J. Buehler, Bioinspired hierarchical composite design using machine learning: Simulation, additive manufacturing, and experiment, *Mater. Horiz.* **5**, 939 (2018).
- [43] M. Grujicic, J. Snipes, and S. Ramaswami, Ballistic-penetration resistance and flexural stiffness optimization of a nacre-mimetic, B4C-reinforced, polyurea-matrix composite armor, *Int. J. Struct. Integr.* **8**, 341 (2017).
- [44] L. de Arcangelis, S. Redner, and H. J. Herrmann, A random fuse model for breaking processes, *J. Phys. Lett.* **46**, 585 (1985).
- [45] S. Zapperi, P. K. V. V. Nukala, and S. Simunovic, Crack roughness and avalanche precursors in the random fuse model, *Phys. Rev. E* **71**, 026106 (2005).
- [46] M. J. Alava, P. K. V. V. Nukala, and S. Zapperi, Statistical models of fracture, *Adv. Phys.* **55**, 349 (2006).
- [47] F. Reurings and M. J. Alava, Damage growth in random fuse networks, *Eur. Phys. J. B* **47**, 85 (2005).
- [48] P. K. V. V. Nukala and S. Simunovic, Statistical physics models for nacre fracture simulation, *Phys. Rev. E* **72**, 041919 (2005).
- [49] P. K. V. V. Nukala and S. Simunovic, A continuous damage random thresholds model for simulating the fracture behavior of nacre, *Biomaterials* **26**, 6087 (2005).
- [50] Editors W. Annicchiarico, J. Periaux, M. Cerrolaza, and G. Winter, *Evolutionary Algorithms and Intelligent Tools in Engineering Optimization*, CIMNE Series of Handbooks (CIMNE, Barcelona, Spain, 2005), ISBN: 1-84564-038-1.
- [51] S. Olariu and A. Y. Zomaya, *Handbook of Bioinspired Algorithms and Applications* (Chapman and Hall/CRC, Boca Raton, 2005), ISBN: 1-58488-475-4.
- [52] D. Ashlock, *Evolutionary Computation for Modeling and Optimization* (Springer, New York, 2006), ISBN: 0-387-22196-4.

- [53] W. Weibull, A statistical distribution function of wide applicability, *J. Appl. Mech.-T. ASME* **18**, 293 (1951).
- [54] S. Pradhan, A. Hansen, and B. K. Chakrabarti, Failure processes in elastic fiber bundles, *Rev. Mod. Phys.* **82**, 499 (2010).
- [55] M. K. Karakasis and K. C. Giannakoglou, On the use of metamodel-assisted, multi-objective evolutionary algorithms, *Eng. Optimiz.* **38**, 941 (2006).
- [56] S. A. Kyriacou, V. G. Asouti, and K. C. Giannakoglou, Efficient PCA-driven EAs and metamodel-assisted EAs, with applications in turbomachinery, *Eng. Optimiz.* **46**, 895 (2014).
- [57] M. Gardner, in *Knotted Doughnuts and Other Mathematical Entertainments* (W.H. Freeman, New York, 1986), Chap. 2.
- [58] <http://velos0.ltt.mech.ntua.gr/easy/>.
- [59] A. Bandivadekar, *On the Road in 2035: Reducing Transportation's Petroleum Consumption and GHG Emissions* (Massachusetts Institute of Technology, Boston, 2008).